

## Investigating the effects of structural parameters on seismic aggravation of two-dimensional sedimentary valleys

Shengyin Qiang<sup>a,b</sup>, Hongwei Wang<sup>a,b</sup>, Ruizhi Wen<sup>a,b,\*</sup>, Qifang Liu<sup>c</sup>, Ying Zhou<sup>d</sup>

<sup>a</sup> Key Laboratory of Earthquake Engineering and Engineering Vibration, Institute of Engineering Mechanics, China Earthquake Administration, Harbin, 150080, China

<sup>b</sup> Key Laboratory of Earthquake Disaster Mitigation, Ministry of Emergency Management, Harbin, 150080, China

<sup>c</sup> School of Civil Engineering, Suzhou University of Science and Technology, Suzhou, 215011, China

<sup>d</sup> School of Civil Engineering, Jilin Jianzhu University, Changchun, 130000, China



### ARTICLE INFO

#### Keywords:

Valley-induced effects  
Seismic ground motion  
Numerical simulations  
Key structural parameters  
Aggravation factors

### ABSTRACT

The valley-induced ground motion amplification has been well-documented and validated in previous studies, however, it remains challenging to fully integrate them into ground motion models, seismic hazard assessment, and engineering practice. In this paper, we first investigate the 2D seismic response in the Mygdonian basin, Greece, and compare the numerical results with comparable studies to validate the feasibility of our numerical toolbox in quantifying ground motion aggravation. In order to orientate towards more generally applicable conclusions rather than a site-specific, 32 idealized three-layered sediment-filled trapezoidal valleys are constructed with reference to the geological structure of the Mygdonian basin, aiming to explore the sensitivity of their additional effects attributes to the subsurface structure parameters of the valley. The half-width of the valley surface is divided into three subregions according to the wave propagation path, similar to the concept of seismic microzonation. The multivariate analysis reveals that the seismic response of each sub-region has differential or even diametrically opposite sensitivity to these structural parameters. The aggravation factor of the valley edge region shows a significant tendency to decrease with increasing edge angle, but poor sensitivity to the shape factor. On the contrary, the aggravation factor of the central region is positively correlated with the shape factor, but largely independent of the valley edge angle. Furthermore, we performed a quantitative statistical analysis and gave a simple correspondence between the seismic aggravation factor and structural parameters for different period intervals, which is an acceptable quantitative scheme from an engineering point of view.

### 1. Introduction

The sediment-filled valleys with complex geological structures have a major impact on the spatial distribution pattern of seismic ground motions and earthquake-induced damage observed in numerous destructive earthquakes [1–3]. The complex amplification patterns of the sedimentary valley can be mainly attributed to the following reasons: (1) the valley (or basin)-edge effect, i.e., the ground motions at the valley edges are amplified due to the constructive interference between edge-generated multiple diffracted/surface waves and transmitted waves arriving through the sediments [4]; (2) earthquake-induced resonance, i.e., the constructive interference of body waves and valley-edge-generated surface waves propagating along vertically or laterally within a valley of limited-size can give rise to one-dimensional (1D) and two-dimensional (2D) resonance patterns [5]; (3) the focusing

effect, i.e., the bowl-shaped geometric configuration of the underlying bedrock focuses energy carried by seismic waves on specific locations within the valley [6]. These pioneering studies have made considerable developments in the 2D, and three-dimensional (3D) numerical simulations and instrumental observation approach to account for seismic site effects over the past few decades. Some early examples include the Mexico City Valley during the 1985 earthquake and Leninakan during the 1988  $M_S$  6.8 earthquake in Armenia, where loose sediments amplified the amplitude of ground motion and extended shaking duration [2, 7,8]. The more intense ground motion experienced in Santa Monica during the 1994  $M_W$  6.7 Northridge earthquake than in neighboring areas due to the lens structure of the basin basement [6,9]. The “basin edge effect” was responsible for an uneven damage belt in Kobe during the 1995  $M$  7.2 Hyogo-ken Nambu earthquake, as proposed by Kawase [4]. Not only that, but the sensitivity and variability of seismic hazard

\* Corresponding author. No. 29 Xuefu Road, Harbin, 150080, China.

E-mail address: [ruizhi@iem.ac.cn](mailto:ruizhi@iem.ac.cn) (R. Wen).

caused by the local site conditions have also been evidenced in 1999 Chi-Chi earthquake [10], Rhône valley in Switzerland [11], 2011  $M_W$  6.2 Christchurch earthquake [12], and 2015 Gorkha earthquake in Kathmandu valley [13].

Since highly populated metropolitan areas lie in river valleys, sedimentary basins and alluvial plains, where the flat terrain facilitates the building and infrastructure, but destructive earthquakes occur from time to time, such as San Francisco Bay Areas, Dinar valley, North China basin, and Kanto basin, to name a few. Any structure, and in particular long-period structures (e.g., tall buildings, bridges, dams, tunnels, and other lifeline engineering systems) will experience huge challenges caused by local site conditions amplifying ground movements and increasing damage for these urban. Most current seismic building codes provisions explicitly allow for the consideration of 1D site effects in the form of a spectral amplification factor, which modifies the amplitude and shape of the elastic response spectra based on site classification defined according to a 1D proxy  $V_{S30}$  ( $V_{S30}$  is time-weighted shear wave velocity over the upper 30 m). However, numerous scholars [14–17] have pointed out that 1D numerical modeling is generally inadequate to represent the seismic response for sediment-filled valleys because they cannot account for the subsurface geometric irregularities and lateral confinement of sedimentary valleys. In recent years, an effective strategy to incorporate the “valley effect” contribution into the building codes is achieved by rescaling the spectral ordinate and period parameters to modify the design spectrum [14,18–20].

Despite the fact that observations provide the most realistic response to site effects, they are restricted by the insufficient number of recordings to be used only for specific study sites. On the other hand, it is extremely difficult, if not impossible, to find a time-domain solution for elastic wave propagation in heterogeneous media with irregular subsurface configurations. In these cases, the numerical approaches are employed almost indispensable to obtain a more realistic estimate of the seismic response. The numerical approaches such as discrete wave-number, finite element, boundary finite element, finite difference, and spectral element method have been used for seismic wavefield synthesis, both perform qualitative and quantitative analysis on idealized models for different geometric structures, soil dynamic properties, as well as in the realistically modeled valleys [18–23]. The 1D site effects commonly underestimate surface amplification patterns compared to the 2D and 3D responses, as it fails to adequately capture the constructive interference direct shear with valley-induced surface waves [24,25]. As we all know that 3D analysis is beneficial, it is not feasible for large areas due to the huge economic demands, computational requirements, extensive input parameters, and general absence of reliable 3D seismic velocity models. In addition, given the complexity and uniqueness of the ground motion characteristics depending on the local site conditions makes it difficult to draw general conclusions that can be applied to a target site. Therefore, it is not common in engineering practice. That is, 2D simulation is expedient at the moment. Under certain conditions, three-dimensional models can be appropriately simplified to two-dimensional models are still useful, if we are interested in site effects [24,26]. Furthermore, 2D simulations play a considerable advantage when statistically analyzing the relationship between amplification effects and characteristic parameters through numerous models. For these reasons, two-dimensional modeling was used in this study.

The present work consists of two main steps. First, we use numerical simulation technique to quantitatively evaluate the seismic response of the Mygdonian basin, a sedimentary valley located in Thessaloniki, Northern Greece. The strong-motion data are considered to be the most realistic representation of site amplification, which could be taken as a measurement standard for the reliability of numerical simulations. We compare simulated and observed waveforms and spectral amplifications to quantify the ground motion aggravation in the Mygdonian valley, as well as illustrate the feasibility of the specific 2D modeling approach in approximating the actual site effects. Following the validation of our numerical toolbox, we discuss the influence of key structural parameters

on aggravation factors in different regions for idealized trapezoidal valleys, which are constructed with different geometric shapes based on the geological profile of the Mygdonian basin. The half-width of the basin ground surface is divided into three parts according to a simplified wave propagation path. We have conducted extensive research on three-layered valleys with homogeneous viscoelastic materials, focusing on the general (rather than site-specific), in a statistical sense, aggravation factor caused by the 2D effects of the valley structure. Nonlinear soil behavior is not covered by our present study, although it may cause changes in resonant frequencies and site amplification due to soil modulus degradation and an increase in hysteresis damping [27].

## 2. Overview of site-specific and computations

### 2.1. Description of Mygdonian basin

The Mygdonian sedimentary basin is a tectonic depression about 30 km northeast of Thessaloniki, Greece, as shown in Fig. 1a. It has a narrow, more symmetrical shape along cross-section A, which is filled with low-velocity sediments that thin from the center to the southern and northern edges of the basin. The width of cross-section A of the Mygdonian basin along the north-northwest-south-southeast direction is almost 6 km, and near the subsidence-related lakes of Langada and Volvi in the west-east direction, respectively. The maximum sediment thickness at the TST station in the central position of basin cross-section A is nearly 200 m. The multidisciplinary European experimental site is a network of three-channel digital accelerographs located in the Mygdonian basin (Fig. 1b), also known as the Euroseistest site (<http://euroseisdb.civil.auth.gr/>). The blue triangles in Fig. 1c represent the strong-motion stations arranged at the ground surface along cross-section A. The stations PRO, PRR, STC and STE are installed on the valley edge with  $V_{S30} = 500\text{--}570$  m/s, corresponding to soil class B; the stations GRA, TST, FRM and BUT on loose sediments in the center of Mygdonian basin with  $V_{S30} = 190\text{--}280$  m/s, corresponding to soil class C, according to the Eurocode 8 [28] classification.

In order to correlate the estimated site effects with the complex underlying geology, Raptakis et al. [16] developed a 2D numerical model of cross-section A based on soil properties and subsurface structures obtained from seismic prospecting and laboratory testing, as listed in Table 1. There are two conditions, the difference between 2D and 3D site effects are small, and the detailed structure of this cross-section has been well validated [26,29,30]. Our numerical modeling is modified from the literature [16] and consists of six layered media (see Fig. 3). The material damping  $\xi$  can be simply formulated as a function of the S-wave quality factor  $Q_S$  (i.e.,  $\xi = 1/2Q_S$ ); the Poisson's ratio describing the elastic properties of the material depends on the P- and S-wave velocities (see Table 1).

### 2.2. Modeling and numerical simulations

In this study, we investigate the effect of surface geology on seismic motion by performing extensive numerical simulations using an explicit finite element method [31]. The dynamic equations of the transmitting nodes on the artificial boundary are calculated by the multi-transmitting formula (MTF) [32,33]. Since the MTF can only simulate the outward scattered wavefield, it is necessary to subtract the incident wavefield from the total wavefield to separate the scattered wavefield when using the MTF to develop the motion equation of the boundary nodes. This solution is subsequently used for the numerical simulation of linear viscoelastic soil behavior in 2D topography models, as well as for 1D analysis [34,35]. The top boundary of the numerical modeling is a free surface, and the second-order MTF is applied to the vertical and bottom boundaries to avoid the interference of reflected waves. Mass and stiffness proportional Rayleigh damping is introduced in the time-domain finite element simulations to achieve an almost constant attenuation value in the frequency range of interest. A constant element size of 5 m is

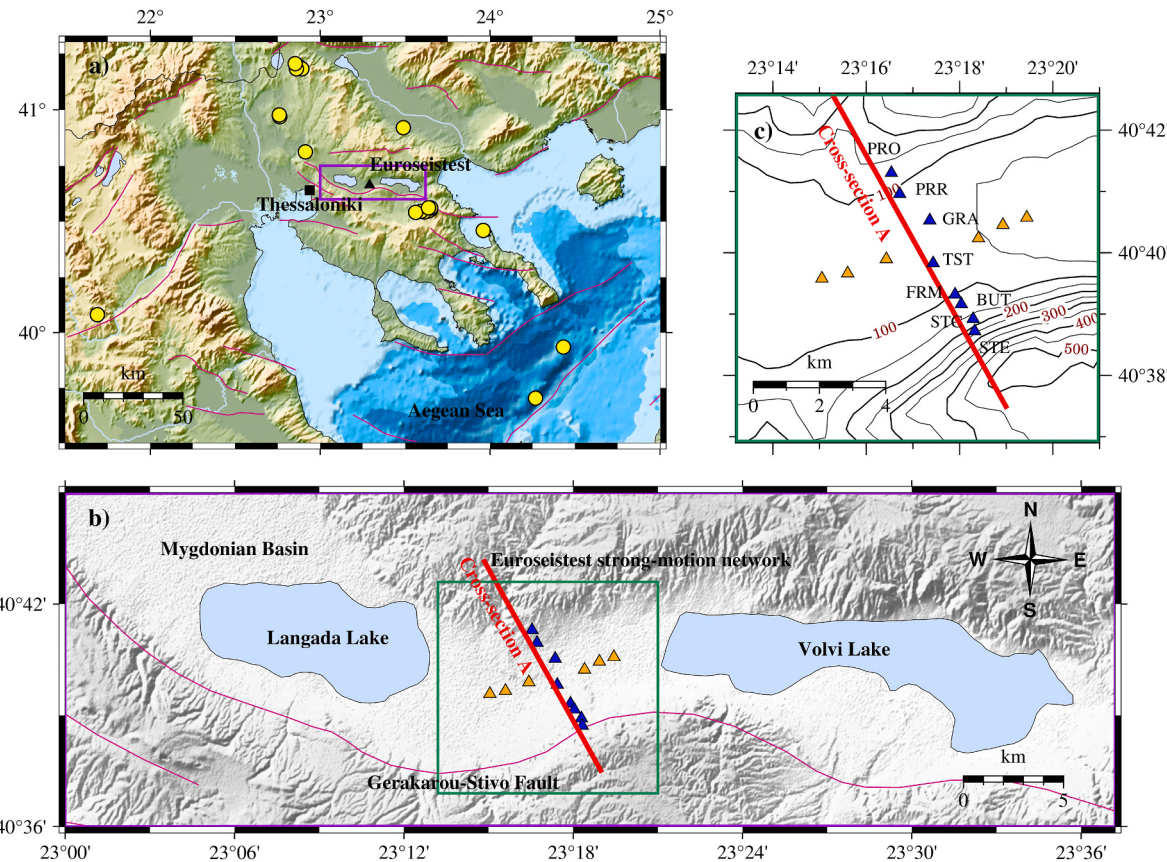


**Fig. 1.** An overview map of the Mygdonian basin. (a) The epicenters of the earthquakes listed in Table 1 are represented by yellow circles. (b) Local topographic map showing the location of the Mygdonian basin between Langada and Volvi lakes. (c) Distribution of the strong-motion stations from the Euroseistest seismic observation network, the stations indicated by blue triangles are used in this study. The modeled cross-section A is denoted by the red solid line.

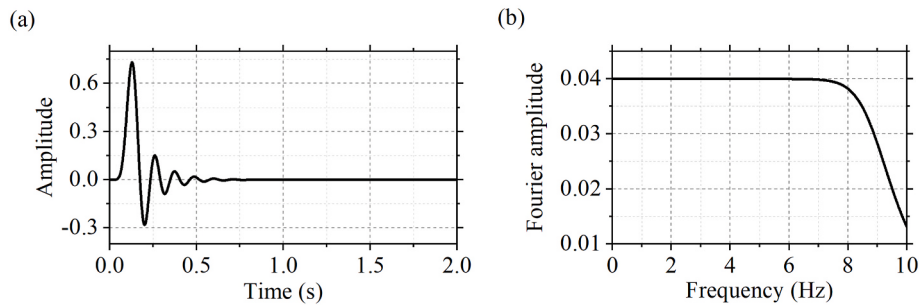


**Fig. 2.** The Gabor pulse used as input time function for the 2D simulation, and the time series (a) and Fourier amplitude spectrum (b) of the pulse are shown.

**Table 1**

Properties of the sediments and basement rock for 2D Euroseistest model (Modified from Raptakis et al. [16]).

Formations	$V_s$ (m/s)	$V_p$ (m/s)	$\rho$ (kg/ $m^3$ )	$Q_s$	$\xi^b$	$v^c$
Sediments	1	200	1500	2150	20	2.50% 0.491
	2	300	1600	2080	30	1.66% 0.481
	3	450	2000	2100	40	1.10% 0.473
	4	650	2500	2150	65°	0.76% 0.463
	5	800	2600	2200	80 <sup>a</sup>	0.63% 0.447
Bedrock	6	2600	4500	2600	200	0.01% 0.249

<sup>a</sup> The quality factor  $Q_s = V_s/10$ .

<sup>b</sup> The dimensionless damping ratio  $\xi = 1/2Q$  for sediments.

<sup>c</sup> Poisson's ratio  $v = (\gamma^2 - 2)/2(\gamma^2 - 1)$ , in which  $\gamma = V_p/V_s$ .

used in both the horizontal and vertical directions, with the element size limited to one-sixth to one-tenth of the minimum wavelength, and a time step of 0.0008 s is determined from the stability conditions. For our calculations, we chose a maximum accurate frequency of 7 Hz, which covers the primary amplification peaks determined in Chávez-García et al. [29]. The wave transformation generated by the plane SV wave incident on the wedge causes the energy partitioning on the two components, which has a smaller 2D effect than an SH wave incidence [14, 22]. Nevertheless, to account for the complex wave mode conversion (e.g., SV to P) induced by valley wedges, only in-plane motion, i.e., vertically propagating plane SV wave, is considered in this work.

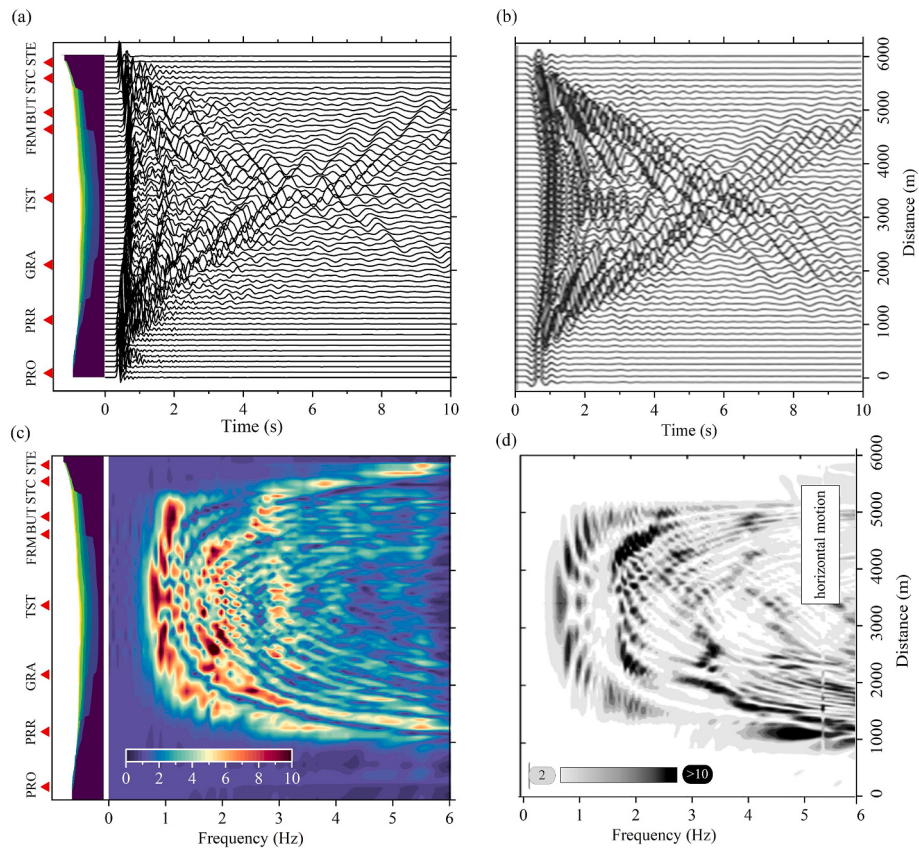


**Fig. 3.** (a) Horizontal component synthetic seismograms of the Euroseistest 2D model, excited with the Gabor pulse along the bottom of the model. (b) Similar as Fig. 3a but derived from Makra and Chávez-García [36]. (c) The amplification functions for each observation receiver on the surface with respect to the receiver at the location of reference station PRO, based on the synthetic time histories in Fig. 3a. (d) Similar as Fig. 3c but derived from Semblat et al. [38].

### 3. Verification of the numerical technique

#### 3.1. Comparison of time and frequency domains

Two-dimensional numerical modeling is applied to investigate the ground motion amplification effect of the Euroseistest site in both time and frequency domains. We used the Gabor pulse as input motion (see Fig. 2) to simplify the excitation and to allow tracking of the multiple reflections, refractions, and mode conversions of the incident pulse in the synthetic wavefield of sedimentary basins. Fig. 3a depicts a synthetic seismogram of the horizontal component consisting of 121 receivers, which are arranged at a constant 50 m interval along the ground surface. It is clear from the synthetic seismogram that profile A itself is dominated by the surface waves generated at the basin edges, leading to a significant increase in the duration of ground motion on the sediment. Similar to previous observations [36], our wavelet-based analysis results adequately characterize the amplification of ground motions due to lateral inhomogeneities, as illustrated by the comparison of Fig. 3a–b. Although there are some slight discrepancies in their wave-trains due to different input motions or modified soil models used in the 2D numerical simulations. The synthetic seismogram also reveals that the higher amplitudes and more complex wavefields are generated on the northern edge compared to the other side. This difference is considerably attributed to gentler sloping angles of the northern edge compared to the southern edge of the Mygdonian basin. This phenomenon was also observed in previous studies by both Chávez-García et al. [29] and Makra et al. [37].

The amplification functions are calculated for each receiver with respect to the reference site (the station PRO), using the synthetic seismogram in Fig. 3a. The spatial distributions of the amplification

functions are shown in Fig. 3c, where the 2D site effects significantly increase the amplification around 0.85 Hz in the central part of the basin, while amplification peaks at higher frequencies (above 1 Hz) on the valley edge. We then compare the calculated transfer functions with the results of Semblat et al. [38] (see Fig. 3c–d), where Gabor and Ricker pulse as an SV excitation, respectively. In general, the distribution patterns of these amplification peaks are compatible, except that our results are lower at frequencies 4–6 Hz, between 1000 and 2000 m. It can be seen from the frequency-distance distribution shows that the peaks are usually close to the southern valley with a steeper edge. The amplitude and distribution patterns of these amplification peaks depend on the tectonics of the Euroseistest site, so the effects of factors such as the edge angle, valley geometry and sediment properties on the seismic response should be discussed later.

#### 3.2. Comparison of spectral amplification ratios

In addition to verifying our numerical results with previous works in both time and frequency domains, we also validate them by comparing valley site amplification derived from instrumental observations and computations. A total of 118 three-component strong-motion recordings of 22 earthquakes are collected from the Euroseistest network, and specific information on these selected earthquake events are summarized in the Electronic Supplement. Before evaluating the site response using the Standard Spectral Ratio (SSR) [39] technique, the acceleration time histories have been processed as done by Wang and Wen [40]. A Konno-Ohmachi function [41] smoothing coefficient  $b = 40$  is applied to the Fourier amplitude spectra.

Observational and computed amplification functions are compared in Fig. 4. The horizontal ground motion captured by the station PRO

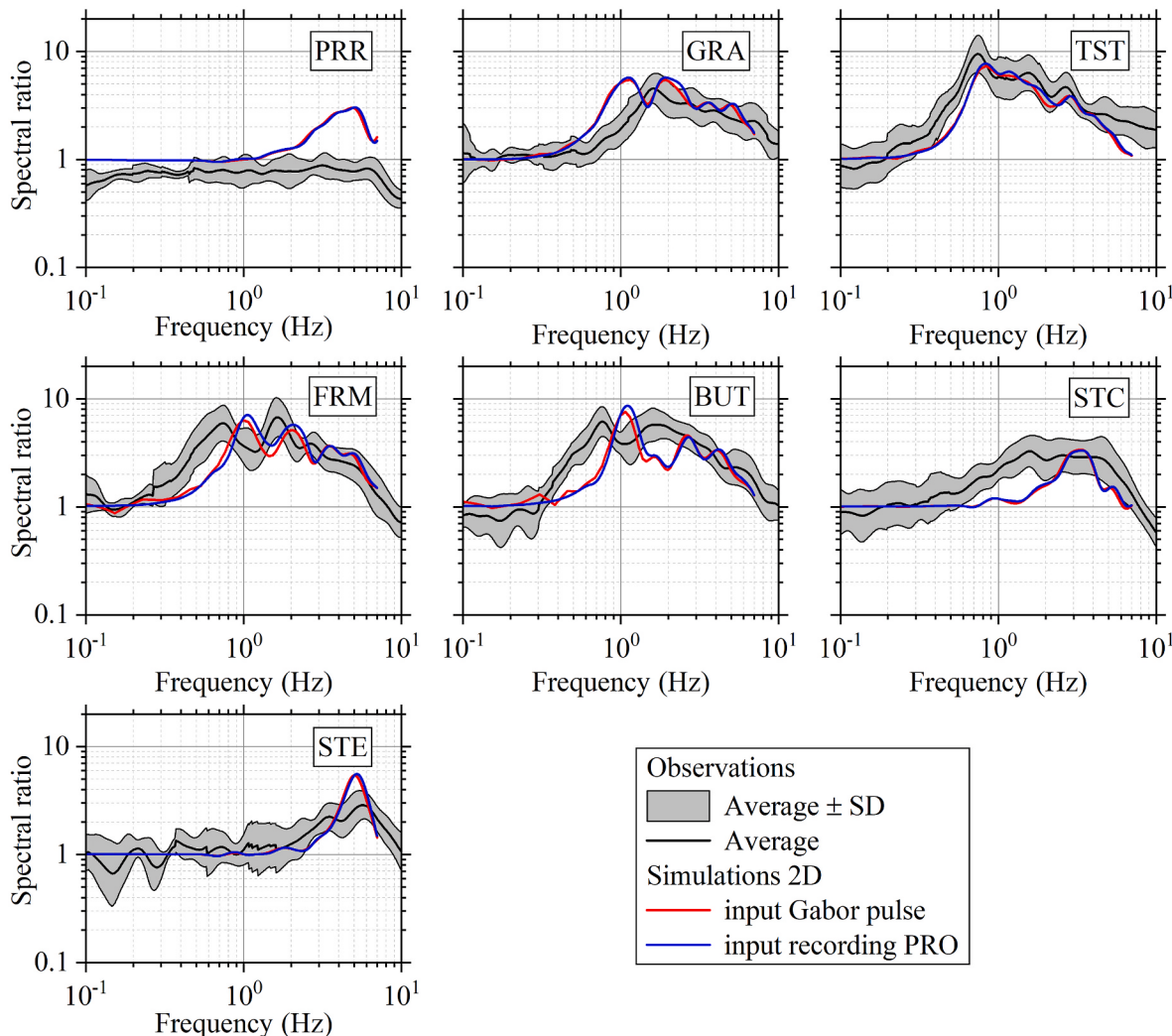


**Fig. 4.** Comparison of average observed and simulated Fourier spectral ratios for Euroseistest site. The station PRO is considered to be a reference site. Shaded areas represent the average observed plus and minus one standard deviation.

during the 13 May 1995  $M_W$  6.5 earthquake is taken for the site-specific input motion for the seismic response analysis. A comparison of the computed and measured accelerograms and Fourier amplitude spectra are shown in Figs. S1 and S2 of the Supplementary Material, respectively. Fig. 4 shows the average spectral ratios and standard deviations of the horizontal component for each station with respect to reference station PRO, as well as the amplification functions of the 2D simulation relative to the station PRO for excitation by both the Gabor pulse and ground motion recording. Generally speaking, the amplification functions have amplitude similar to the SSR curves of the observations at most frequency bands. The station TST site in the central part of the valley has a significant low-frequency (about 0.7 Hz) amplification and can be as high as 10, where it corresponds to the deepest sediments in the basin. Stations GRA, FRM and BUT have moderate amplification values of almost 4–7 times at frequencies 1–3 Hz, whereas the stations STC and STE at the south edge of the basin that appear slightly amplified and shift to higher frequencies. However, when comparing our results to those of earlier studies [37,42], it must be pointed out that our results are in general agreement with them except for the lower spectral ratios observed at the stations STC and STE. From this perspective, the 2D simulation results provide an approximate description of the spectral magnification trend of the observation, although our 2D model does not capture all the peaks and troughs of the frequency response. In other words, the agreement with the measured signals is satisfactory,

examining the reliability of the numerical approach in reproducing realistic seismic motions.

#### 4. Sensitivity analysis of key structural parameters

We compare numerical simulations and ground surface observations to demonstrate the reliability of our 2D theoretical approach in reconstructing realistic earthquake scenarios in the Mygdonian basin. Our numerical results exhibit a relatively satisfactory agreement in predicting the field observations, at least from an engineering design practice point of view. The Mygdonian valley is an excellent case for studying near-surface sedimentary structures on the modification of ground motion, where the well-known stratigraphic structure allows us to correlate the geometric configuration and dynamic properties of the 2D valley with the site response results obtained from the numerical analysis. For this reason, this section investigates the sensitivity of the ground-motion aggravation effect to key geometric characteristic parameters through a series of idealized symmetric trapezoidal valleys.

##### 4.1. Idealized modeling and 2D/1D aggravation factors

For the sake of simplicity, we constructed the simplified models with three horizontally stratified sediments using the Mygdonian basin as a reference model, which is to some extent more realistic and

representative of the actual site than a single overburden, even if it's assumed. The mechanical property values of the idealized models were calculated from the 2D soil structure of the Mygdonian basin, using a time-weighted algorithm (see Table 2). The valley width ( $w$ ), total sediment depth ( $d$ ) and edge angle ( $\alpha$ ) of the valley are set as variables, and their selected values are summarized in Table 3. The thickness of each layer has a fixed proportion (1/3) as the total sediment depth varies. Finally, a total of 32 2D valley models with different subsurface geometries were constructed by permutation and combination  $w$ ,  $d$  and  $\alpha$ , as shown schematically in Fig. 5.

For consistency reasons, the synthetic time histories for receivers along the valley surface are obtained using the same simulation method as before, excited with the Gabor wavelet (see Fig. 2). The numerical transfer functions of the 2D and 1D simulations for each surface receiver can be calculated from the output over the input in the frequency domain. Furthermore, the Fourier spectra of the eight seismograms in Table 4 are convolved with the transfer functions at each receiver, and then an inverse Fourier transform is performed to obtain the acceleration time histories for all receivers on the surface of the valleys. Final, a total of 512 (32\*8\*2 = 512) cases were investigated using numerical technique in this work. Eight acceleration time histories were selected as input motions from the Pacific Earthquake Engineering Research Center Ground-Motion Database (<https://ngawest2.berkeley.edu/>). They are required to be observed from bedrock or stiff soil sites ( $V_{S30} \geq 760$  m/s) and have a good signal-to-noise ratio in the frequency band of interest [43]. The 475 years return period design spectrum for site classes A (Type 1) recommended in the EC8 was used to match the unscaled accelerograms. Baseline corrected and fourth-order Butterworth filtered with low-cut frequencies of 10.0 Hz are pre-processed for the selected input strong-motion recordings. The accelerograms and corresponding 5% damped normalized acceleration response spectra of the selected strong-motion recordings are given in Supplementary Material Figs. S3 and S4.

The aggravation factor, it is defined as the spectral amplification due to the complex 2D/3D site effects over the 1D response of the soil columns as proposed by Chávez-García and Faccioli [14], and widely adopted in subsequent studies ([37,44–50]; among many others). In this study, we used the ratio of the 5% damped pseudo-spectral acceleration between the 2D and the corresponding 1D simulations as the aggravation factor. A period- and location-dependent aggravation factor [49,50] is introduced to account for the variability of ground shaking due to local site effects. The MAF( $T/T_0, x/w$ ) of the position for each receiver ( $x$ ) on the free surface for every input motion (R1 ... R8) can be expressed as follows,

$$MAF(T/T_0, x/w) = \frac{PSA_{2D}(T/T_0, x/w)}{PSA_{1D}(T/T_0, x/w)}, \quad (1)$$

where  $PSA_{2D}(T/T_0, x/w)$ ,  $PSA_{1D}(T/T_0, x/w)$  represent the 5% damped pseudo-spectral accelerations of 2D and 1D simulations, respectively;  $T_0$  is the fundamental period of the 1D soil column in the maximum thickness profile of the valley;  $MAF(T/T_0, x/w)$  is a non-dimensional period- and location-dependent aggravation factor.

The maximum aggravation factor MAF for each subregion (i.e., edge region, near-edge region and central region) of the valleys can be calculated from Equation (2)

**Table 2**  
Properties of the sediments and basement rock for idealized valley models.

Description	$V_s$ (km/s)	$V_p$ (km/s)	$\rho$ (kg/ $m^3$ )	$Q_s$	$\xi$	$v$
Loose silty clayey	260	1560	2050	26	1.92%	0.486
Silty-sand mixtures	580	2340	2130	58	0.86%	0.467
Weathered schist and gneiss	875	2750	2250	88	0.57%	0.444
Granite basement	2600	4500	2600	200	0.25%	0.249

**Table 3**  
Geometric parameters of the idealized 2D valley models.

Width (m)		Depth (m)				Edge angle (°)			
$w_1$	$w_2$	$d_1$	$d_2$	$d_3$	$d_4$	$\alpha_1$	$\alpha_2$	$\alpha_3$	$\alpha_4$
2500	5000	100	200	300	400	20	40	60	80

$$MAF = \exp \left[ \frac{1}{n} \sum_{i=1}^n \ln(PLAF(T/T_0, x/w)) \right], \quad (2)$$

where MAF represents maximum value of geometric mean aggravation factor  $MAF(T/T_0, x/w)$  in the period of  $T \leq 1.5T_0$  for each subregion, as recommended in Riga et al. [46] and Zhu et al. [49,50] that the aggravation effect is most affected within the period about  $1.0T_0 \sim 1.5T_0$ ;  $i$  denotes the number of receivers on the ground surface belonging to the corresponding subregion;  $n$  is the total number of receivers within valley edge region, near-edge region, and central region, respectively.

The spatial variability of seismic motion is caused by vertical and lateral inhomogeneities of the valley [4,14–16], and the site response may be overestimated or underestimated in some areas if quantified by a constant. In the practical application of this work, it is considered necessary to identify regions of homogeneous seismic behavior based on Snell's Law involved in the propagation of seismic waves. This procedure is similar to the seismic microzonation in the Taipei basin, Mexico City basin, and Santiago basin, etc. Hence, Fig. 6 depicts the half-width of the valley is divided into three parts of the edge region ( $w_{ed}$ ), the near-edge region ( $w_{ne}$ ) and the central region ( $w_{ce}$ ) intended to investigate the sensitivity of regionally related aggravation effects to the characteristic parameters. The subregion  $w_{ne}$  is derived from Snell's law to determine the approximate area of possible constructive interference among the refracted body waves, direct body waves, and surface waves caused by the valley edge. According to the seismic wave propagation within the valley wedge, three subregions are defined as

$$w_{ed} = \frac{d}{\tan \alpha} \quad (3)$$

$$w_{ne} = d \tan \left( \alpha - \arcsin \left( \frac{V_{S, sediment}}{V_{S, bedrock}} \sin \alpha \right) \right), \quad (4)$$

$$w_{ce} = 0.5w - w_{ed} - w_{ne}, \quad (5)$$

Where  $w_{ed}$ ,  $w_{ne}$ ,  $w_{ce}$  represent the widths of the valley edge, near-edge, and central regions, respectively. Other parameters are illustrated in Fig. 6.

As shown in Fig. 7 represents the sensitivities of the period- and location-dependent amplification factor  $MAF(T/T_0, x/w)$  to structural parameters edge angle of the valley wedge, sediment thickness, and valley width. The shape factor ( $Sf$ ) is defined as the largest sediment depth over the width of the valley (i.e.,  $Sf = d/w$ ), which is usually introduced as a practical and applicable metric to measure the variation of the amplification effect caused by these size factors. Each row shows the distribution of the  $MAF(T/T_0, x/w)$  along non-dimensional period  $T/T_0$  and location  $x/w$  with constant  $\alpha = 40^\circ$ ,  $Sf = 0.06$ , and  $w = 2500$  m for selected valleys, respectively. The amplification factor  $MAF(T/T_0, x/w)$  in the inner region of the valley shows an overall increasing trend with the deepening of the deposition thickness while the decrease of the valley width, and the maximum aggravation points move from the edge to the center of the valley (see Fig. 7a). It is noteworthy that the valley edge about  $x/w = -0.5 \sim -0.4$  where MAF at most periods is below 1.0, suggesting that the de-amplification with respect to the corresponding 1D estimation. This finding is in accordance with the numerical results reported by Riga et al. [46], Zhu et al. [50] and Gelagoti et al. [51], but differs from the studies by Hasal and Iyisan [45], and Khanbabazadeh and Iyisan [52]. This discrepancy is attributed to the different reference

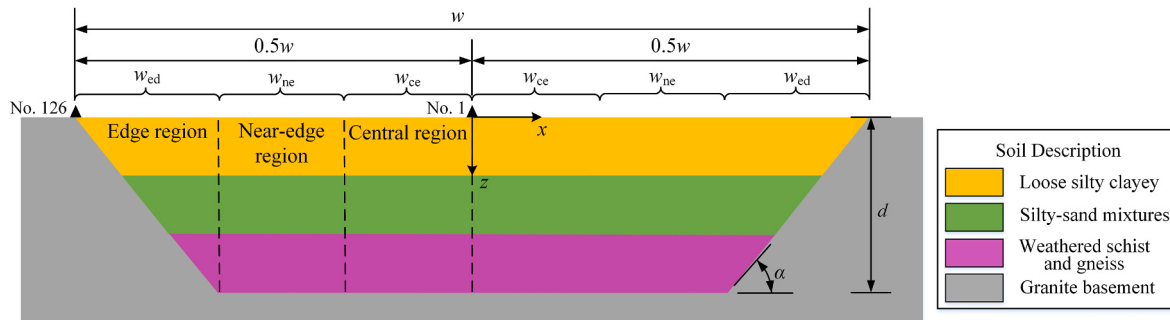


**Fig. 5.** Geometry of the simplified 2D alluvial valley. The symbols  $w$ ,  $d$  and  $\alpha$  represent the valley width, deposition thickness, and edge angle. The valley is divided into the valley edge ( $w_{\text{ed}}$ ), the near-edge region ( $w_{\text{ne}}$ ) and the central region ( $w_{\text{ce}}$ ), respectively.

**Table 4**

Parameters about the selected strong-motion recordings used for analysis.

No.	ID	Event	Data (yyyy-mm-dd)	Station	$M_W$	$R_{\text{rup}}$ (km)	$V_{S30}$ (m/s)
R1	804	Loma Prieta	1989-10-18	So. San Francisco, Sierra Pt.	6.93	63.15	1020.6
R2	1587	Chi-Chi, Taiwan	1999-09-20	TTN042	7.62	65.25	845.3
R3	1613	Duzce, Turkey	1999-11-12	Lamont 1060	7.14	25.88	782.0
R4	3324	Chi-Chi, Taiwan-06	1999-09-25	HWA002	6.30	51.83	789.2
R5	5650	Iwate, Japan	2008-06-13	IWTH18	6.90	64.27	891.5
R6	5670	Iwate, Japan	2008-06-13	MYG011	6.90	82.93	1423.8
R7	6041	El Mayor -Cucapah, Mexico	2010-04-04	San Diego Road Dept	7.2	110.95	827.0
R8	8167	San Simeon, CA	2003-12-22	Diablo Canyon Power Plant	6.52	37.97	1100.0

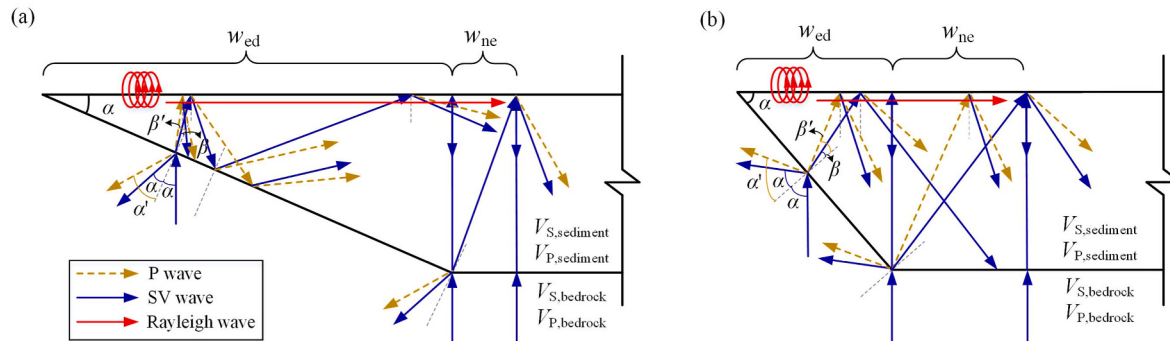


**Fig. 6.** Schematic illustration of the seismic wave propagation in the edge region of the valley with different edge angles. (a) Inside a gentle and (b) steep valley wedge.  $\alpha$  and  $\alpha'$  represent the reflection angles of the SV and P waves, the incidence angle is the same as the reflection angle for SV wave, as well as equal to the sloping edge of the valley wedge.  $\beta$  and  $\beta'$  represent the transmission angles of SV and P waves. For incidence and transmission angles,  $\alpha' = \arcsin[(V_{P,\text{bedrock}}/V_{S,\text{bedrock}})\cdot\sin\alpha]$ ,  $\beta = \arcsin[(V_{S,\text{sediment}}/V_{S,\text{bedrock}})\cdot\sin\alpha]$ ,  $\beta' = \arcsin[(V_{P,\text{sediment}}/V_{S,\text{bedrock}})\cdot\sin\alpha]$ , in which,  $V_{S,\text{bedrock}}, V_{P,\text{bedrock}}$  are the shear and compression wave velocities of the bedrock, and  $V_{S,\text{sediment}}, V_{P,\text{sediment}}$  are the ones for sediment.

sites selected for the 1D simulations, i.e., the 2D/1D aggravation factor quantifies the 2D additional effect relative to the location of the local 1D soil profile or edge rock outcrop. The central region exhibits an approximate 1D seismic response for a valley that is both widest and shallowest, which is mainly attributable to the surface waves attenuating more rapidly with distance than the incoming body waves. In addition, Fig. 7 shows that the seismic response in the center of the valley with  $Sf \leq 0.04$  has almost no deviation from the 1D response and is not contaminated by valley effects. A generalized evaluation of Fig. 7b and c show that the influence of edge angle on the aggravation effect for 2D response is slightly compared to the shape factor. Furthermore, an overview of the period (corresponding 1D profile at each site) and location-dependent suggests that the valley-induced amplification or de-amplification effects are mainly distributed in three subregions, which supports our previous ideas about seismic microzonation.

#### 4.2. Effect of valley edge angle ( $\alpha$ )

We performed a multivariate statistical analysis to investigate the influence of valley edge angle on the aggravation effect of ground motion within different subregions. Fig. 8a shows the cumulative histograms of the aggravation factor MAFs grouped by edge angle. The derived distribution indicates that the computed MAF values mostly fluctuate around 1.5 for subregions  $w_{\text{ne}}$  and  $w_{\text{ce}}$ , while they are more dispersed in the subregion  $w_{\text{ed}}$ . Regarding the MAFs of each subregion of valleys with different edge angles, the valley edge aggravation effect is significantly enhanced as the slope of the wedge becomes gentler. The histograms were fitted with Gaussian, log-normal and Weibull distributions, and we found that the log-normal distribution was identified as the best fit, as shown in Fig. 8a. To analyze MAF variability, both selected independent variables (i.e., edge angle  $\alpha$ , and shape factor  $Sf$ ) are considered simultaneously for multivariate analysis. Thus, the MAFs within each subregion are categorized by shape factor  $Sf$  as 0.02–0.04, 0.06–0.08, and 0.12–0.16, respectively. The correlation of the

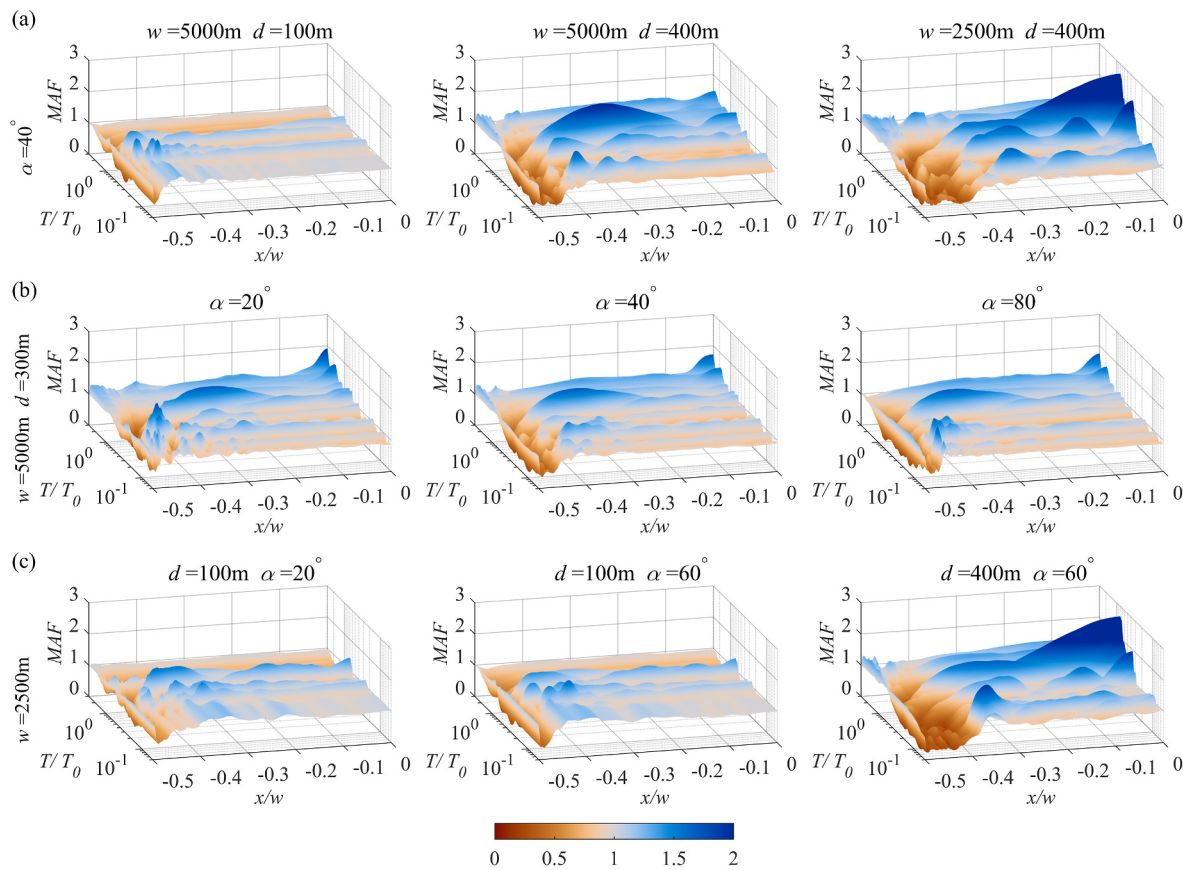


**Fig. 7.** Aggravation factor  $MAF(T/T_0, x/w)$  versus the half-width of the valley surface and the period normalized to the fundamental period  $T_0$  for selected valleys with the same geometric parameters. (a)  $\alpha = 40^\circ$ , (b)  $w = 5000\text{ m}$ ,  $d = 300\text{ m}$  and (c)  $w = 2500\text{ m}$ .  $x/w = 0$  represents the center of the valley,  $x/w = -0.5$  represents the location of the sediment-bedrock interface at the valley wedge.

aggravation factor MAF with the valley edge angle  $\alpha$  for each subregion and their nonlinear best-fitting are also illustrated in Fig. 8b. The aggravation factor MAFs for each region were regressed against  $\alpha$  by the nonlinear least-squares fitting of the form as,

$$\ln(MAF) = a + b \ln(\alpha), \quad (6)$$

where  $a$  and  $b$  represent the regression coefficients.

It can be seen from Fig. 8b that aggravation factors MAFs in the valley edge region  $w_{ed}$  of the valley wedge exhibit a tendency to decrease for increasing edge angle  $\alpha$ . The maximum value of MAFs for region  $w_{ed}$  is as high as 2.10 when the edge angle  $\alpha$  is  $20^\circ$ , while conspicuously decreasing to 0.66–1.41 for the case of the edge angle above  $60^\circ$ . On the other hand, we performed a nonlinear fit between MAFs and  $\alpha$  values for region  $w_{ed}$ , calculating the values of coefficients of determination at different shape factors (0.02–0.04, 0.06–0.08 and 0.12–0.16, in that order), that is, 0.436, 0.749 and 0.802, respectively. For the subregion  $w_{ed}$ , there is a significant inverse correlation between the aggravation factor MAF and edge angle  $\alpha$  regardless of the set of shape factors. However, we must point out that our results are not consistent with the previous view of Riga [53], and Zhu and Thambiratnam [54], whose studies concluded that the effect of edge angle on the seismic aggravation factor is not significant. The multivariate statistical analysis allows us to examine the independent effects of several control variables ( $\alpha$ ,  $Sf$ , and  $T_0$ ) on the observed variable MAF, to investigate the correlation between edge angle  $\alpha$  and shape factor  $Sf$ , as well as their simultaneous effects on the MAF. From this perspective, the key structural parameters controlling the local surface amplification effects are usually interdependent, for example, the most unfavorable situation for the valley subregion  $w_{ed}$  occurs in the combination of the smallest edge angle and

the largest shape factor.

For the valley edge, the 2D seismic response caused by the valley structure is suppressed relative to the 1D ground response analysis for some situations. This observation can be explained by the physical mechanisms involved in seismic wave propagation, for the in-plane case, the incident wave refracts at the bedrock-sediment interface and then propagates towards the near-edge region, together with experiencing wave mode conversion. A similar pattern has been reported by Moczo et al. [22]. The aforementioned phenomena are even more pronounced for steep edge angles, which can be explained by sketches of the seismic wave propagation in very gentle and steep wedges, respectively (Fig. 6). For gently sloping valleys (Fig. 6a), the aggravation factor MAF is generally greater than that of other regions because the incident waves are allowed to be reflected multiple times in the wedge with a gentle slope, and it is more opportunity for constructive interference with the surface waves, refracted waves and scattered waves generated at the valley wedge. As described in Fig. 6b for the case of a very steep valley, the incident angle  $\alpha$  of the seismic wave increases along with steeper slopes in the valley, and most of the energy carried by the incident seismic waves propagates directly outside the region  $w_{ed}$  (i.e., the subregions  $w_{ne}$  and  $w_{ce}$ ) after only once or twice refractions within the valley wedge. In this case, the probability of interference between Rayleigh surface waves and direct or refracted body waves is greatly reduced. Therefore, the steep valleys have a significantly lower MAF for subregion  $w_{ed}$  than for  $w_{ne}$ , possibly even smaller than that for the subregion  $w_{ce}$ . We refer to this physical phenomenon as the “blind area” effect of seismic wave interference.

Similar to the  $w_{ed}$  subregion, the same form of nonlinear fits between MAF and  $\alpha$  were also performed for the  $w_{ed}$  and  $w_{ne}$  subregions, respectively. The coefficients of determination corresponding to the log-

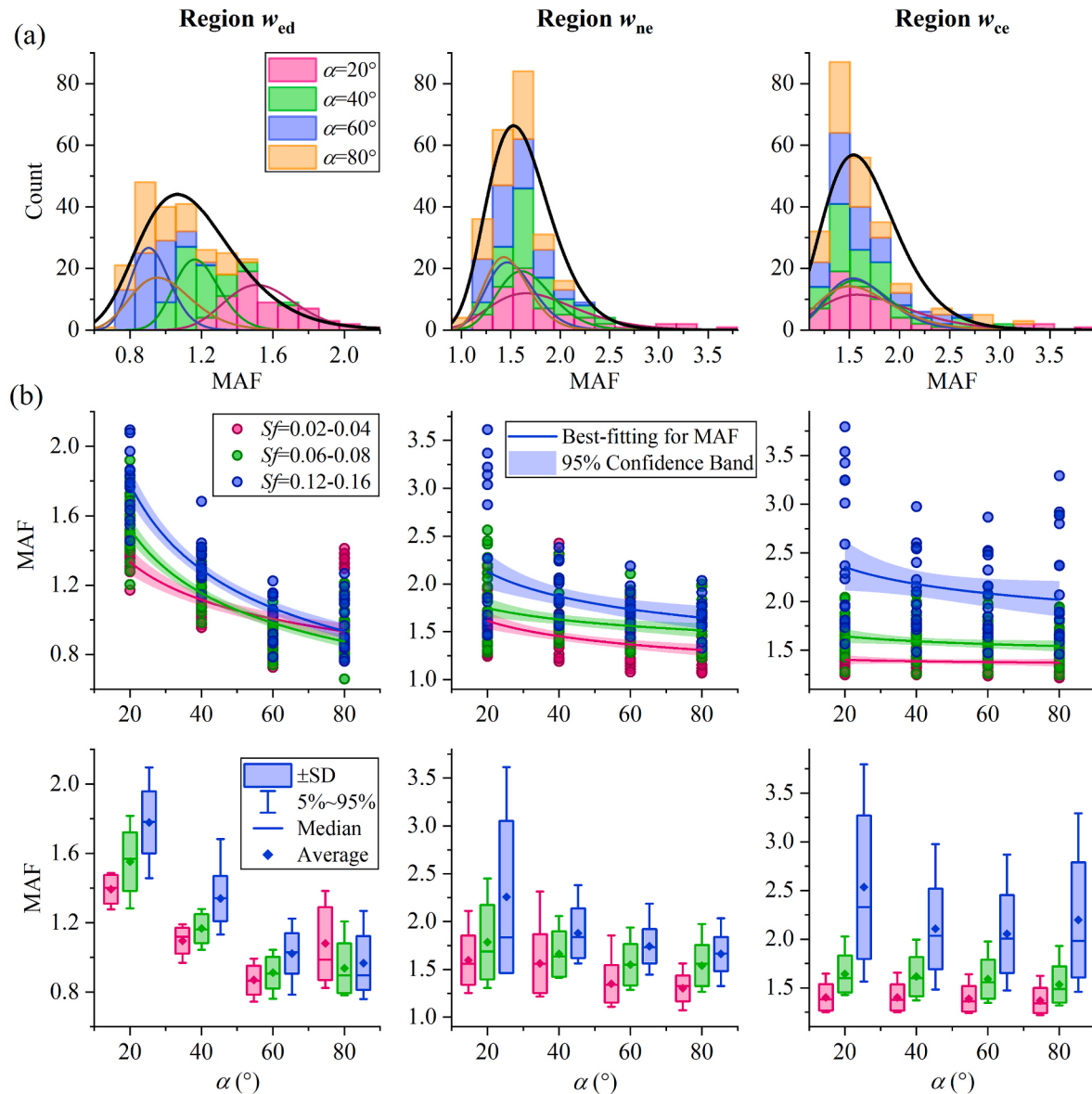


**Fig. 8.** Influence of valley edge angle  $\alpha$  on aggravation factor MAF for valley edge region  $w_{ed}$ , near edge region  $w_{ne}$  and central region  $w_{ce}$ . (a) Histograms of MAF values for the three subregions by type of edge angle. (b) MAFs versus edge angle  $\alpha$ . The MAFs within each subregion are categorized by shape factor  $S_f$  as 0.02–0.04, 0.06–0.08 and 0.12–0.16. The lines represent the nonlinear best-fitting between MAF and  $\alpha$  for subregions  $w_{ed}$ ,  $w_{ne}$  and  $w_{ce}$  respectively.

linear regression analysis of both two subregions are quite low (less than 0.3), indicating that the ground motion characteristics are almost independent of the edge angle for the central part of the valley. Distinct from the valley edge, the distribution pattern of the aggravation factor with  $\alpha$  is more heterogeneous and disordered in the near-edge and central regions. This variance is also demonstrated in the plus and minus one standard deviation of aggravation factors. The grouped boxplots (Fig. 8b) show that the MAFs gradually converge with increasing  $\alpha$  for the subregion  $w_{ne}$ , but there is no discernible trend for the subregion  $w_{ce}$ . We can say that for both the subregions  $w_{ne}$  and  $w_{ce}$ , their 2D/1D seismic aggravation effects are largely independent of the edge angle variable, although the  $w_{ne}$  subregion is slightly affected by changes in edge angle. Consistent findings have been observed for both single and multiple horizontally stratified sediment-filled valleys [46,55]. Compared to the region  $w_{ed}$ , the amplification effects are generally higher in the  $w_{ne}$  and  $w_{ce}$  regions, especially for the type of valleys with larger shape factor. The analysis considering two key structural parameters simultaneously shows that  $S_f$  plays a more important role in changing the amplification effect in both regions, which will be focused on later.

#### 4.3. Effect of shape factor ( $S_f$ )

The distribution of aggravation factors MAFs for subregions  $w_{ed}$ ,  $w_{ne}$  and  $w_{ce}$  in relation to the valley shape factor  $S_f$  and their nonlinear best-fitting are shown in Fig. 9. The regression analysis between MAFs and  $S_f$  is performed using the same form of the least squares method as that of edge angle  $\alpha$ . The cumulative histogram of MAFs classified into three groups according to  $S_f$  is depicted in Fig. 9a. The fitting curves of the log-normal distribution between MAF and  $S_f$  show that its mean values gradually increase with increasing  $S_f$ , while the standard deviation has a tendency to decrease with increasing shape factor. When examining the effect of  $S_f$  on MAFs, they are categorized according to  $\alpha$  and plotted in different colors as shown in Fig. 9b. As revealed by the distribution of MAFs along the  $S_f$  in the subregion  $w_{ed}$ , the aggravation effect is more pronounced for a valley edge slope of  $20^\circ$ , which is attributed to the energetic diffraction effect induced by the long-distance effects [55]. The best-fit curve between MAF and shape factor  $S_f$  show that their correlation deteriorates with increasing  $\alpha$  in the subregion  $w_{ed}$ , since the coefficients of determination are 0.460, 0.440, 0.229 and 0.175 in that

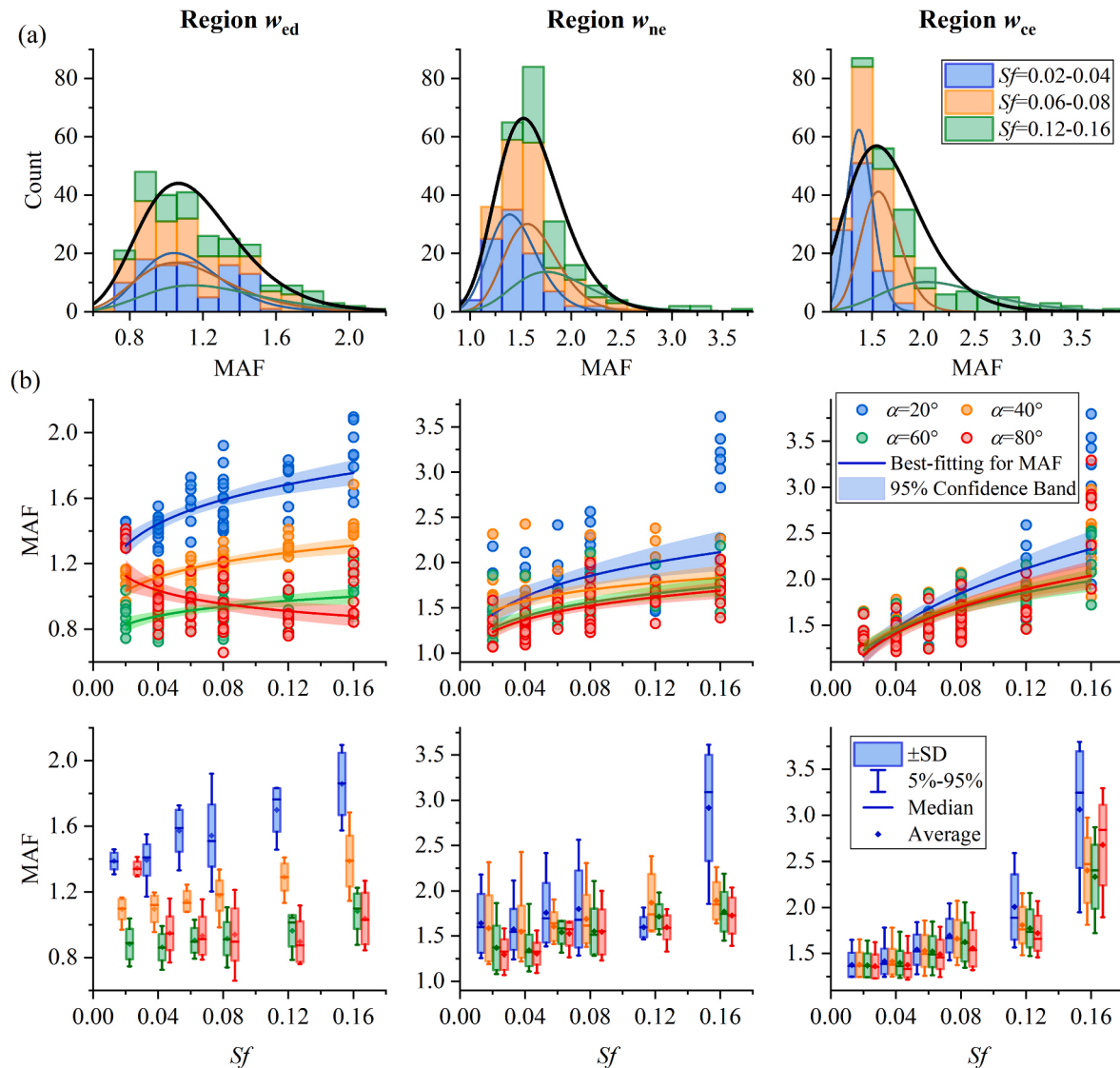


**Fig. 9.** Influence of shape factor  $S_f$  on aggravation factor MAF for valley edge region  $w_{ed}$ , near edge region  $w_{ne}$  and central region  $w_{ce}$ . (a) Histograms of MAF values for the three subregions by type of shape factor. (b) MAFs versus shape factor  $S_f$ . The MAFs within each subregion are categorized by edge angle  $\alpha$  as  $20^\circ$ ,  $40^\circ$ ,  $60^\circ$  and  $80^\circ$ . The lines represent the nonlinear best-fitting between MAF and  $S_f$  for subregions  $w_{ed}$ ,  $w_{ne}$  and  $w_{ce}$  respectively.

order with increasing  $\alpha$ . We used multivariate statistical analysis to confirm that the shape factor still slightly influences of wedge zone aggravation pattern, especially for the case of the gentle valleys ( $\alpha < 45^\circ$ ). This phenomenon was not captured in the previous examination by Riga et al. [46]. Nevertheless, it is not as significant as the edge angle parameter for subregion  $w_{ed}$ .

The shape factor has an overall relatively pronounced effect on the aggravation factors in the subregions  $w_{ne}$  and  $w_{ce}$ , with coefficients of determination of 0.3–0.4 and 0.5–0.6 for best-fit lines, respectively. Loose sediments at the upper part of the bedrock intensify the seismic response of subregions  $w_{ne}$  and  $w_{ce}$  of the valley with the increasing shape factor. It can be seen from the coefficients of determination that the correlation between  $S_f$  and MAF strengthens as the edge angle becomes gentler for subregion  $w_{ce}$ . It is noteworthy that for the valley with the gentlest sloping edge and the largest shape factor, the maximum aggravation factor is observed for all subregions. More specifically, the MAF can be as high as 3.8 at the central region of the valley with constant  $S_f = 0.16$  and  $\alpha = 20^\circ$ , which may be due to the interference of the vertically propagating SV waves with secondary surface waves, or to the constructive interference of Rayleigh waves excited by both edges of the valley when they propagate along the surface to both near-edge and

central regions. This type of valley configuration is the most unfavorable for seismic protection. By contrast, 2D response gently amplified (about 30%) with respect to the corresponding 1D response in the case of smallest shape ratio, owing to the considerable attenuation of surface waves as they propagate along the surface towards the interior of the valley. The dispersion of the aggravation factors MAFs for the central region grows noticeably as the shape factor increases. In addition, the behavior of the ground surface also dependent on the source term, i.e., the frequency content of the input motion is close to the fundamental period of the site resulting in a substantial enhancement of the additional effect.

#### 4.4. Quantitative statistical analysis of MAFs

There is a consensus that the relationship between valley-induced ground motion amplification and controlling parameters is explored through sufficiently comprehensive parametric studies [18,29,43,44,55,56]. Previous experience has focused on measuring the difference between one- and two-dimensional modeling by deriving a constant or a period-dependent aggravation factor (or equivalent indicator) from numerical simulations of real basins or idealized models [14–18,46–52].

In this work, we performed a descriptive statistical analysis and gave a simple correspondence between the seismic aggravation factor MAF and structural parameters for different period intervals, which is an acceptable quantitative scheme from an engineering point of view.

The aggravation spectra usually display a significant non-uniformity, with their intermediate periods typically corresponding to higher levels of aggravation effects compared to those of lower and higher periods, instead of covering the entire periods. For this reason, it is allowed to separate the aggravation factor of the whole period range into four period intervals, namely,  $0-0.4T_0$ ,  $0.4T_0 - 0.8T_0$ ,  $0.8T_0 - 1.2T_0$ , and  $1.2T_0 - 1.6T_0$ . They are considered to cover the range of typical periods of the additional effects of the 2D seismic response with respect to the 1D response. Fig. 10 illustrates the three-dimensional representation of the multidimensional relationships between MAF,  $\alpha$ , and  $Sf$  for each subregion of the valleys that are categorized by the dimensionless period  $T/T_0$  (i.e.,  $0 < T/T_0 \leq 0.4$ ,  $0.4 < T/T_0 \leq 0.8$ ,  $0.8 < T/T_0 \leq 1.2$ , and  $1.2 < T/T_0 \leq 1.6$ ). The main features are the following.

$T_0 \leq 1.6$ ). The main features are the following.

- For the subregion  $w_{ed}$ , the aggravation factor MAF decreases with increasing edge angles  $\alpha$  and decreasing shape factor  $Sf$  for each period interval. It is observed that in general and for most valley models MAF for shorter period with  $T \leq 0.8T_0$  is greater than those for longer period.
- For the subregion  $w_{ne}$ , the trend of MAF is similar to that of the subregion  $w_{ed}$ , except that the maximum values of MAF usually lies in the intermediate periods with  $0.4T_0 < T \leq 1.2T_0$ .
- For the subregion  $w_{ce}$ , MAF was observed to increases with increasing  $Sf$  for all periods. The additional effect of the intermediate period predominates the ground motion response at the center of the valley compared to the long and short periods.

Table 5 gives the statistical results of the average  $\pm$  one standard

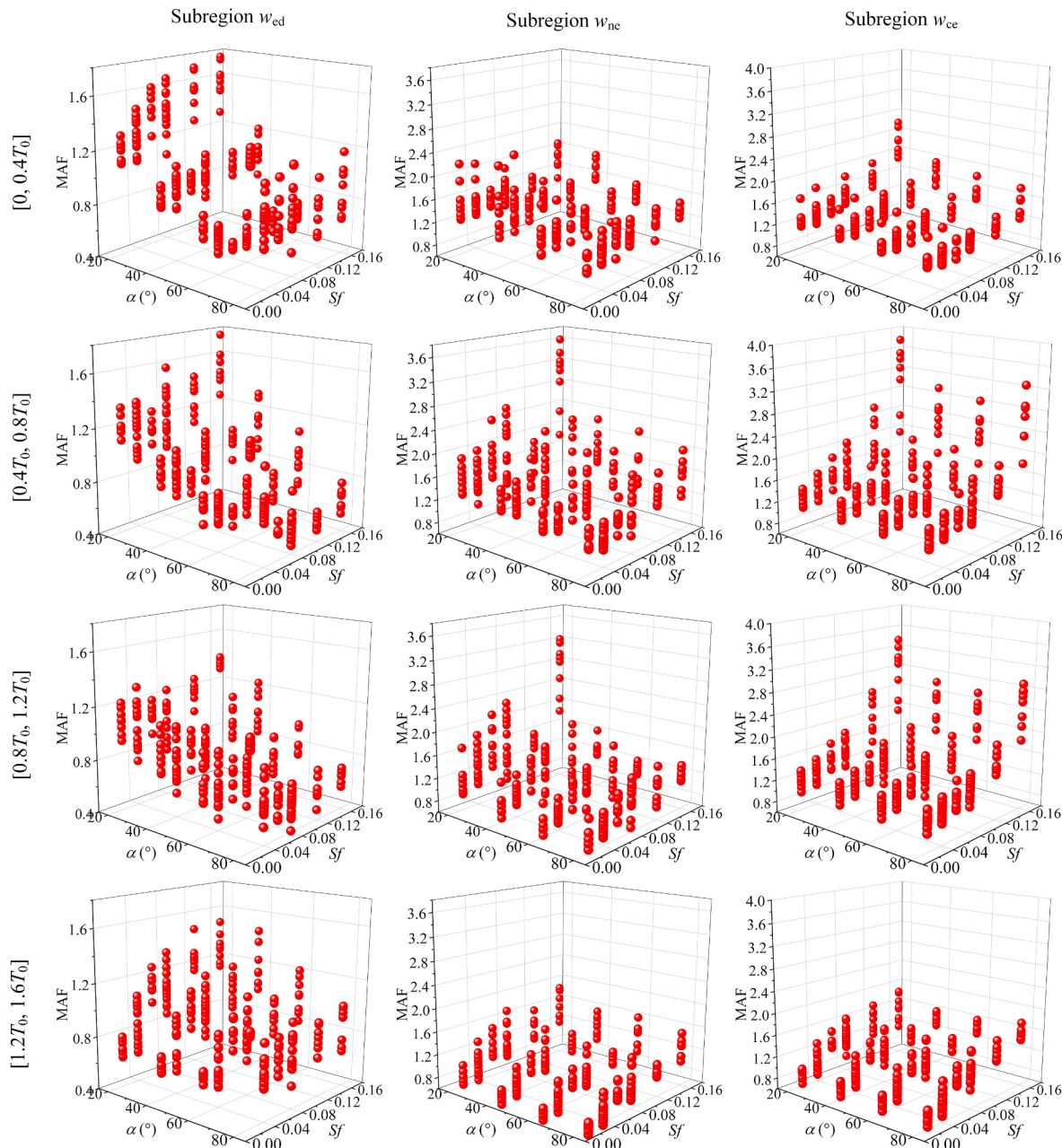


Fig. 10. Three-dimensional distribution relationships among the aggravation factor MAF, edge angle  $\alpha$ , and shape factor  $Sf$  for each subregion ( $w_{ed}$ ,  $w_{ne}$ , and  $w_{ce}$ ) of the valleys.

**Table 5**

Statistical results of the effect of structural parameters  $\alpha$  and  $Sf$  on MAF in each subregion that are expressed in terms of period interval categorization.

	$\alpha <$	Subregion $w_{ed}$		Subregion $w_{ne}$		Subregion $w_{ce}$	
		$Sf < 0.1$	$Sf > 0.1$	$Sf < 0.1$	$Sf > 0.1$	$Sf < 0.1$	$Sf > 0.1$
[0, $0.4T_0]$	$\alpha <$	1.15	1.29	1.49	1.65	1.33	1.76
	$45^\circ$	$\pm 0.23$	$\pm 0.29$	$\pm 0.24$	$\pm 0.20$	$\pm 0.16$	$\pm 0.31$
	$\alpha >$	0.81	0.74	1.33	1.42	1.27	1.44
	$45^\circ$	$\pm 0.23$	$\pm 0.16$	$\pm 0.17$	$\pm 0.15$	$\pm 0.13$	$\pm 0.16$
[0.4T_0, $0.8T_0]$	$\alpha <$	1.04	1.23	1.50	1.99	1.38	2.27
	$45^\circ$	$\pm 0.18$	$\pm 0.22$	$\pm 0.35$	$\pm 0.67$	$\pm 0.23$	$\pm 0.67$
	$\alpha >$	0.76	0.70	1.24	1.58	1.35	2.07
	$45^\circ$	$\pm 0.19$	$\pm 0.14$	$\pm 0.23$	$\pm 0.24$	$\pm 0.21$	$\pm 0.54$
[0.8T_0, $1.2T_0]$	$\alpha <$	0.95	1.14	1.27	1.69	1.31	2.13
	$45^\circ$	$\pm 0.15$	$\pm 0.17$	$\pm 0.36$	$\pm 0.66$	$\pm 0.20$	$\pm 0.56$
	$\alpha >$	0.74	0.73	1.02	1.15	1.28	1.99
	$45^\circ$	$\pm 0.17$	$\pm 0.12$	$\pm 0.23$	$\pm 0.20$	$\pm 0.18$	$\pm 0.48$
[1.2T_0, $1.6T_0]$	$\alpha <$	0.90	1.20	0.93	1.29	1.08	1.42
	$45^\circ$	$\pm 0.19$	$\pm 0.15$	$\pm 0.25$	$\pm 0.23$	$\pm 0.24$	$\pm 0.20$
	$\alpha >$	0.81	0.92	0.84	1.13	1.08	1.45
	$45^\circ$	$\pm 0.14$	$\pm 0.14$	$\pm 0.22$	$\pm 0.19$	$\pm 0.24$	$\pm 0.14$

deviation of the aggravation factor MAF within each subregion, which are expressed in terms of period interval categorization. First of all, it should be noted that different levels of seismic amplification occur in most cases, except for the expected de-amplification within the subregion  $w_{ed}$  when the valley boundary becomes steeper (i.e.,  $\alpha \gg 45^\circ$ ). Our results compared with those of Riga et al. [46] and Uzielli et al. [56] indicate that their proposed coefficients are relatively conservative (about 0.90–1.14), which is attributed to the flatter edge angles (the maximum edge angle of the valley edge is  $61^\circ$ – $65^\circ$ ) used in the numerical experiments. The maximum MAFs found in the near-edge regions of the valley with  $Sf < 0.1$  is 1.50, similar to the aggravation factors of the Norcia basin (Italy) obtained by Rodriguez-Plata et al. [23], equal to 1.4–1.5. At the center of the valley, the average  $\pm$  one standard deviation of the MAFs is as high as  $2.27 \pm 0.67$  for models with  $Sf > 0.1$  and a period interval of  $0.4T_0 < T < 0.8T_0$ , meaning that the 2D additional effects caused by the valley configuration is more than doubled compared to the 1D site response. The considerable standard deviation implies that the aggravation factor exhibits significant dispersion, which is quite insensitive to the valley geometry, individual characteristics of the input motion, and other parameters. In the central part of the valleys with small shape factors, the 2D seismic response is not completely degraded to the corresponding 1D response, instead of being amplified by about 30% (see Table 5).

An overall assessment is that the mean values of MAF in this study are compatible with the ranges obtained in other comparable studies, for which values of 2.0 by Raptakis et al. [57], 2–3 by Makra et al. [44], 1.4–1.7 by Paolucci and [58], 1.1–2.5 by Chen et al. [59], 0.79–1.87 by Riga et al. [46], 1.2–1.7 by Madiai et al. [60], 1.3–1.8 by Zhu et al. [50], and of 0.8–2.0 were obtained by Uzielli et al. [56]. Another important point to mention is that the mean values of MAFs in the subregion  $w_{ce} > w_{ne} > w_{ed}$  for valleys with shape factor  $Sf > 0.1$ , while  $w_{ne} > w_{ce} > w_{ed}$  for valleys with shape factor  $Sf < 0.1$ . On the whole, the strongest aggravation effects of the near-edge region are generally found in shorter period intervals, while they tend to show up in longer periods in the central part of the valley.

## 5. Conclusions

The valley-induced ground motion amplification and structural damage have been well observed and examined in numerous historical earthquakes. However, the design parameters derived from current seismic codes do not take sufficiently into consideration complex phenomena on site response induced by complex structures, and for these reasons should be improved. In these cases, the 2D numerical methods

are employed almost as an estimation to obtain a more realistic estimate of the dynamic behavior. In this study, we first investigated the effects of surface geology on the seismic ground motions of the Mygdonian basin both in time and frequency domains. The computational results are in good agreement with the spectral magnification trend of the observations at most stations, and similar behaviors have been found in previous studies. Our numerical toolbox performs satisfactorily both the quantification of ground motion aggravation and the feasibility of a 2D modeling approach in approximating the actual site effects, at least from an engineering design practice point of view.

Until the numerical approaches have been validated, we expect to explore the sensitivity of the valley-induced ground amplification effect on the structural parameters. A total of 32 idealized trapezoidal valleys were assumed with reference to the geometric configuration of the Euroseistest site, which were filled with three horizontally layered sediments and shaped by three key geometric parameters (valley width, sediment depth, and edge angle). For engineering purposes, the period- and location-dependent aggravation factor MAF is defined as the ratio of the pseudo-acceleration response spectra between 2D and corresponding 1D simulations along the valley. The valley half-width is divided into three subregions with homogeneous seismic behavior according to the seismic wave propagation path, that is, edge region  $w_{ed}$ , near-edge region  $w_{ne}$  and central region  $w_{ce}$ .

We use multivariate analysis to investigate the sensitivity of several seismic ground motion characteristics to important structural parameters. The seismic response in the valley edge region is progressively reduced with increasing edge angle because the incident seismic waves propagate beyond the edge region after only a few refractions within the steeper wedge. The amplification in areas far from the valley edge (subregions  $w_{ne}$  and  $w_{ce}$ ) is hardly affected by the edge angle. For the case of steep wedges, the de-amplification effect ( $< 1.0$ ) of 2D seismic response compared to 1D response is commonly observed in subregion  $w_{ed}$ , which is known as the blind area effect. The shape factor has a relatively pronounced effect on the aggravation factor in the near-edge region  $w_{ne}$  and central region  $w_{ce}$ , where the aggravation effect enhancement for increasing shape factor. In order to be oriented to engineering practice, we performed a descriptive statistical analysis and gave a simple correspondence between the seismic aggravation factor and structural parameters for different period intervals, which is considered to be a widely acceptable quantitative scheme. It is observed that for the central part of valleys with  $Sf > 0.1$ , the valley-induced amplification can be up to 100% with respect to the corresponding 1D response, and such drastic ground motion amplification should be given sufficient attention in engineering design, ground motion models, earthquake hazard and risk mitigation. Furthermore, this study accounts for the dependence of the aggravation factor on the structural parameters, period, and subregion, and gives a simple correspondence among them.

## CRediT author statement

**Shengyin Qiang:** Conceptualization, Computation, Original draft. **Hongwei Wang:** Methodology, Formal analysis, Writing- reviewing & editing, Funding acquisition. **Ruiwei Wen:** Conceptualization, Supervision, Funding acquisition, Writing- reviewing & editing. **Qifang Liu:** Software, Validation. **Ying Zhou:** Writing- reviewing & editing.

## Declaration of competing interest

The authors declare that they have no known competing financial interests or personal relationships that could have appeared to influence the work reported in this paper.

## Data availability

Data will be made available on request.

## Acknowledgments

The authors would like to thank the anonymous reviewers for their valuable comments that improved this article. Strong ground motion recordings used in this study were downloaded from the web portal of the EUROSEISTEST at <http://euroseisdb.civil.auth.gr>. This work was supported by Scientific Research Fund of Institute of Engineering Mechanics, China Earthquake Administration (Grant No. 2021EEVL0202), National Natural Science Foundation of China (Grant No. 51978434).

## Appendix A. Supplementary data

Supplementary data to this article can be found online at <https://doi.org/10.1016/j.soildyn.2023.107964>.

## References

- [1] Sanchez-Sesma FJ. Site effects on strong ground motion. *Soil Dynam Earthq Eng* 1987;6(2):124–32. [https://doi.org/10.1016/0267-7261\(87\)90022-4](https://doi.org/10.1016/0267-7261(87)90022-4).
- [2] Bard PY, Campillo M, Chávez-García FJ, Sánchez-Sesma F. The Mexico earthquake of September 19, 1985—a theoretical investigation of large- and small-scale amplification effects in the Mexico City Valley. *Earthq Spectra* 1988;4(3):609–33. <https://doi.org/10.1193/1.1585493>.
- [3] Trifunac MD. Site conditions and earthquake ground motion—A review. *Soil Dynam Earthq Eng* 2016;90:88–100. <https://doi.org/10.1016/j.soildyn.2016.08.003>. 2016.
- [4] Kawase H. The cause of the damage belt in Kobe: “The basin-edge effect”, constructive interference of the direct S-wave with the basin-induced diffracted/Rayleigh waves. *Seismol Res Lett* 1996;67(5):25–34. <https://doi.org/10.1785/gssrl.67.5.25>.
- [5] Bard PY, Bouchon M. The two-dimensional resonance of sediment-filled valleys. *Bull Seismol Soc Am* 1985;75(2):519–41. <https://doi.org/10.1785/BSA0750020519>.
- [6] Gao S, Liu H, Davis PM, Knopoff L. Localized amplification of seismic waves and correlation with damage due to the Northridge earthquake: evidence for focusing in Santa Monica. *Bull Seismol Soc Am* 1996;86(1B):S209–30. <https://doi.org/10.1785/BSSA08601BS209>.
- [7] Kawase H. Time-domain response of a semi-circular canyon for incident SV, P, and Rayleigh waves calculated by the discrete wavenumber boundary element method. *Bull Seismol Soc Am* 1988;78(4):1415–37. <https://doi.org/10.1785/BSSA0780041415>.
- [8] Borcherd R, Glassmoyer G, Andrews M, Cranswick E. Effect of site conditions on ground motion and damage. *Earthq Spectra* 1989;5(1S):23–42. <https://doi.org/10.1193/1.1585233>.
- [9] Graves RW, Pitarka A, Somerville PG. Ground-motion amplification in the Santa Monica area: effects of shallow basin-edge structure. *Bull Seismol Soc Am* 1998;88(5):1224–42. <https://doi.org/10.1785/BSSA0880051224>.
- [10] Lee SJ, Chen HW, Ma KF. Strong ground motion simulation of the 1999 Chi-Chi, Taiwan earthquake from a realistic three-dimensional source and crustal structure. *J Geophys Res Solid Earth* 2007;112(B06):B06307. <https://doi.org/10.1029/2006JB004615>.
- [11] Havenith H, Fäh D, Alvarez-Rubio S, Roten D. Response spectra for the deep sediment-filled Rhône valley in the Swiss alps. *Soil Dynam Earthq Eng* 2009;29(1):17–38. <https://doi.org/10.1016/j.soildyn.2008.01.016>.
- [12] Guidotti R, Stupazzini M, Smerzini C, Paolucci R, Ramieri P. Numerical study on the role of basin geometry and kinematic seismic source in 3D ground motion simulation of the 22 February 2011  $M_W$  6.2 Christchurch earthquake. *Seismol Res Lett* 2011;82(6):767–82. <https://doi.org/10.1785/gssrl.82.6.767>.
- [13] Asimaki D, Mohammadi K, Mason HB, Adams KR, Rajaei S, Khadka D. Observations and simulations of basin effects in the Kathmandu valley during the 2015 Gorkha, Nepal, earthquake sequence. *Earthq Spectra* 2017;33(51):35–53. <https://doi.org/10.1193/013117eqs022m>.
- [14] Chávez-García FJ, Faccioli E. Complex site effects and building codes: making the leap. *J Seismol* 2000;4:23–40. <https://doi.org/10.1023/A:1009830201929>.
- [15] Riepl J, Zahradník J, Plicka V, Bard PY. About the efficiency of numerical 1-D and 2-D modelling of site effects in basin structures. *Pure Appl Geophys* 2000;157:319–42. <https://doi.org/10.1007/s002400500002>.
- [16] Raptakis D, Chávez-García FJ, Makra K, Pitilakis K. Site effects at Euroseistest—I. Determination of the valley structure and confrontation of observations with 1D analysis. *Soil Dynam Earthq Eng* 2000;19(1):1–22. [https://doi.org/10.1016/S0267-7261\(99\)00025-1](https://doi.org/10.1016/S0267-7261(99)00025-1).
- [17] Gaudiosi I, Francesco DM, Giuliano M, Marco T. Site effects in the Aterno River Valley (L’Aquila, Italy): comparison between empirical and 2D numerical modelling starting from April 6th 2009  $M_w$  6.3 earthquake. *Bull Earthq Eng* 2014;12:697–716. <https://doi.org/10.1007/s10518-013-9540-6>.
- [18] Vessia G, Russo S. Relevant features of the valley seismic response: the case study of Tuscan Northern Apennine sector. *Bull Earthq Eng* 2013;11(5):1633–60. <https://doi.org/10.1007/s10518-013-9456-1>.
- [19] Cauzza C, Faccioli E, Costa G. 1D and 2D site amplification effects at Tarcento (Friuli, NE Italy), 30 years later. *J Seismol* 2011;15:1–17. <https://doi.org/10.1007/s10950-010-9202-y>.
- [20] Faccioli E, Vanini M. Complex seismic site effects in sediment-filled valleys and implications on design spectra. *Prog Struct Eng Mater* 2003;5(4):223–38. <https://doi.org/10.1002/pse.156>.
- [21] Gelagoti F, Kourkoulis R, Anastasopoulos I, Gazetas G. Nonlinear dimensional analysis of trapezoidal valleys subjected to vertically propagating SV waves. *Bull Seismol Soc Am* 2012;102(3):999–1017. <https://doi.org/10.1785/0120110182>.
- [22] Moczo P, Kristek J, Bard PY, Stripajová S, Hollender F, Chovanová Z, Kristeková M, Sicilia D. Key structural parameters affecting earthquake ground motion in 2D and 3D sedimentary structures. *Bull Earthq Eng* 2018;16(6):2421–50. <https://doi.org/10.1007/s10518-018-0345-5>.
- [23] Rodriguez-Plata R, Ozcebe AG, Smerzini C, Lai GC. Aggravation factors for 2D site effects in sedimentary basins: the case of Norcia, central Italy. *Soil Dynam Earthq Eng* 2021;149:106854. <https://doi.org/10.1016/j.soildyn.2021.106854>.
- [24] Poursartip B, Kallivokas LF. Model dimensionality effects on the amplification of seismic waves. *Soil Dynam Earthq Eng* 2018;113:572–92. <https://doi.org/10.1016/j.soildyn.2018.06.012>.
- [25] Ayoubi P, Mohammadi K, Asimaki D. A systematic analysis of basin effects on surface ground motion. *Soil Dynam Earthq Eng* 2021;141:106490. <https://doi.org/10.1016/j.soildyn.2020.106490>.
- [26] Marrara F, Suhadolc P. 2-D modeling of site effects along the EURO-SEISTEST array (Volvi graben, Greece). *Pure Appl Geophys* 2001;158(12):2369–88. <https://doi.org/10.1007/PL00001175>.
- [27] Miao Y, He H, Liu H, Wang S. Reproducing ground response using in-situ soil dynamic parameters. *Earthq Eng Struct Dynam* 2022;51(10):2449–65. <https://doi.org/10.1002/eqe.3671>.
- [28] European Committee for Standardization (CEN). Eurocode 8: design of structures for earthquake resistance – Part 1: general rules, seismic actions and rules for buildings. European Standard EN 1998-1: 2004 2004.
- [29] Chávez-García FJ, Raptakis D, Makra K, Pitilakis K. Site effects at Euroseistest—II. Results from 2D numerical modeling and comparison with observations. *Soil Dynam Earthq Eng* 2000;20(1):23–39. [https://doi.org/10.1016/S0267-7261\(99\)00026-3](https://doi.org/10.1016/S0267-7261(99)00026-3).
- [30] Manakou M, Raptakis D, Chávez-García FJ, Apostolidis P, Pitilakis K. 3D soil structure of the Mygdonian basin for site response analysis. *Soil Dynam Earthq Eng* 2010;30(11):1198–211. <https://doi.org/10.1016/j.soildyn.2010.04.027>.
- [31] Liao ZP. A finite element method for near-field wave motion in heterogeneous materials. *Earthq Eng Eng Vib* 1984;4(2):1–14 [in Chinese].
- [32] Liao ZP, Wong HL. A transmitting boundary for the numerical simulation of elastic wave propagation. *Soil Dynam Earthq Eng* 1984;4(3):174–83. [https://doi.org/10.1016/0261-7277\(84\)90033-0](https://doi.org/10.1016/0261-7277(84)90033-0).
- [33] Liao ZP, Wong HL, Yang BP, Yuan YF. A transmitting boundary for transient wave analysis. *Sci Sin* 1984;27(10):1063–76. <https://doi.org/10.1360/ya1984-27-10-1063>.
- [34] Ding HP, Yu YY, Zheng ZF. Effects of scarp topography on seismic ground motion under inclined P waves. *Rock Soil Mech* 2017;38(6):1716–24 [in Chinese].
- [35] Yu YY, Ding HP, Liu QF. Effects of impedance ratio between basin sediment and surrounding rock on seismic ground motions and basin-induced Rayleigh waves. *Chin J Geotech Eng* 2020;42(4):667–77 [in Chinese].
- [36] Makra K, Chávez-García FJ. Site effects in 3D basins using 1D and 2D models: an evaluation of the differences based on simulations of the seismic response of Euroseistest. *Bull Earthq Eng* 2016;14:1177–94. <https://doi.org/10.1007/s10518-015-9862-7>.
- [37] Makra K, Raptakis D, Chávez-García FJ, Pitilakis K. Site effects and design provisions: the case of Euroseistest. *Pure Appl Geophys* 2001;158:2349–67. <https://doi.org/10.1007/PL00001174>.
- [38] Semblat JF, Khan M, Parara E, Bard PY, Pitilakis K, Makra K, Raptakis D. Seismic wave amplification: basin geometry vs soil layering. *Soil Dynam Earthq Eng* 2005;25:529–38. <https://doi.org/10.1016/j.soildyn.2004.11.003>.
- [39] Borcherd R. Effects of local geology on ground motion near San Francisco Bay. *Bull Seismol Soc Am* 1970;60(1):29–61. <https://doi.org/10.1785/BSA0600010029>.
- [40] Wang H, Wen R. Attenuation and basin amplification revealed by the dense ground motions of the 12 July 2020  $M_5.1$  tangshan, China, earthquake. *Seismol Res Lett* 2021;92(4):2109–21. <https://doi.org/10.1785/0220200400>.
- [41] Kono K, Ohmachi T. Ground-motion characteristics estimated from spectral ratio between horizontal and vertical components of microtremor. *Bull Seismol Soc Am* 1998;88(1):228–244. <https://doi.org/10.1785/BSSA0880010228>.
- [42] Raptakis D, Theodoulidis N, Pitilakis K. Data analysis of the euroseistest strong motion array in Volvi (Greece): standard and horizontal-to-vertical spectral ratio techniques. *Earthq Spectra* 1998;14(1):203–24. <https://doi.org/10.1193/1.1585996>.
- [43] Kristek J, Moczo P, Bard PY, Hollender F, Stripajová S. Computation of amplification factor of earthquake ground motion for a local sedimentary structure. *Bull Earthq Eng* 2018;16(6):2451–75. <https://doi.org/10.1007/s10518-018-0358-0>.
- [44] Makra K, Chávez-García FJ, Raptakis D, Pitilakis K. Parametric analysis of the seismic response of a 2D sedimentary valley: implications for code implementations of complex site effects. *Soil Dynam Earthq Eng* 2005;25(4):303–15. <https://doi.org/10.1016/j.soildyn.2005.02.003>.
- [45] Hasal ME, Iyisan R. A numerical study on comparison of 1D and 2D seismic responses of a basin in Turkey. *Am J Civ Eng* 2014;2(5):123–33. <https://doi.org/10.11648/j.ajce.20140205.11>.

- [46] Riga E, Makra K, Pitilakis K. Aggravation factors for seismic response of sedimentary basins: a code-oriented parametric study. *Soil Dynam Earthq Eng* 2016;91:116–32. <https://doi.org/10.1016/j.soildyn.2016.09.048>.
- [47] Hasal ME, Iyisan R, Yamanaka H. Basin edge effect on seismic ground response: a parametric study for duzce basin case, Turkey. *Arabian J Sci Eng* 2018;43: 2069–81. <https://doi.org/10.1007/s13369-017-2971-7>.
- [48] Ozaslan B, Iyisan R, Hasal ME, Khanbabazadeh H, Yamanaka H. Assessment of the design spectrum with aggravation factors by 2D nonlinear numerical analyses: a case study in the Gemlik Basin, Turkey. *Bull Earthq Eng* 2022;20:1371–95. <https://doi.org/10.1007/s10518-021-01296-6>.
- [49] Zhu C, Riga E, Pitilakis K, Zhang J, Thambiratnam D. Seismic aggravation in shallow basins in addition to one-dimensional site amplification. *J Earthq Eng* 2020;24(9):1477–99. <https://doi.org/10.1080/13632469.2018.1472679>.
- [50] Zhu C, Thambiratnam D, Gallage C. Statistical analysis of the additional amplification in deep basins relative to the 1D approach. *Soil Dynam Earthq Eng* 2018;104:296–306. <https://doi.org/10.1016/j.soildyn.2017.09.003>.
- [51] Gelagoti F, Kourkoulis R, Anastopoulos I, Tazoh T, Gazetas G. Seismic wave propagation in a very soft alluvial valley: sensitivity to ground-motion details and soil nonlinearity, and generation of a parasitic vertical component. *Bull Seismol Soc Am* 2010;100(6):3035–54. <https://doi.org/10.1785/0120100002>.
- [52] Khanbabazadeh H, Iyisan R. A numerical study on the 2D behavior of the clayey basins. *Soil Dynam Earthq Eng* 2014;66:31–41. <https://doi.org/10.1016/j.soildyn.2014.06.029>.
- [53] Riga E. New elastic spectra, site amplification factors and aggravation factors for complex subsurface geology, towards the improvement of EC8. Greece: Ph.D. Dissertation, Aristotle University of Thessaloniki; 2015.
- [54] Zhu C, Thambiratnam D. Interaction of geometry and mechanical property of trapezoidal sedimentary basins with incident SH waves. *Bull Earthq Eng* 2016;14: 2977–3002. <https://doi.org/10.1007/s10518-016-9938-z>.
- [55] Stambouli AB, Bard PY, Chaljub E, Moczo P, Kristek J, Stripajova S, Durand C, Zendagui D, Derras B. 2D/1D aggravation factors: from a comprehensive study to estimation with a neural network model. In: 16th European conference of earthquake engineering. Thessaloniki, Greece; 2018.
- [56] Uzielli M, Facciorusso J, Madiai C. Statistical calibration of two-dimensional seismic aggravation effects for homogeneous basins. *Soil Dynam Earthq Eng* 2022; 163:107533. <https://doi.org/10.1016/j.soildyn.2022.107533>.
- [57] Raptakis D, Makra K, Anastasiadis A, Pitilakis K. Complex site effects in Thessaloniki (Greece): II. 2D SH modelling and engineering insights. *Bull Earthq Eng* 2004;2(3):301–27. <https://doi.org/10.1007/s10518-004-3803-1>.
- [58] Paolucci R, Morstabili L. Non-dimensional site amplification functions for basin edge effects on seismic ground motion. Third international symposium on the effects of surface geology on seismic motion. 2006. Grenoble, France.
- [59] Chen G, Jin D, Zhu J, Shi J, Li X. Nonlinear Analysis on seismic site response of Fuzhou basin, China. *Bull Seismol Soc Am* 2005;105(2A):928–49. <https://doi.org/10.1785/0120140085>.
- [60] Madiai C, Facciorusso J, Gargini E. Numerical modeling of seismic site effects in a shallow alluvial basin of the Northern Apennines (Italy). *Bull Seismol Soc Am* 2017;107(5):2094–105. <https://doi.org/10.1785/0120160293>.